Emulator-assisted nuclear density-functional-theory inference and its consequences for the structure of neutron stars

Pietro Klausner,[1,2,3,*] Marco Antonelli,[1,†] Gianluca Colò,[2,3,‡] Francesca Gulminelli,[1,4,§] Xavier Roca-Maza,[2,3,5,6,‖] and Enrico Vigezzi[3,¶]

[1] *Université de Caen Normandie, CNRS/IN2P3, LPC Caen (UMR6534), 14050 Caen, France*
[2] *Dipartimento di Fisica "Aldo Pontremoli", Università degli Studi di Milano, 20133 Milano, Italy*
[3] *INFN, Sezione di Milano, 20133 Milano, Italy*
[4] *Institut Universitaire de France, Paris, France*
[5] *Departamento de Física Quàntica i Astrofísica, Martí i Franqués, 1, 08028 Barcelona, Spain*
[6] *Institut de Ciències del Cosmos, Universitat de Barcelona, Martí i Franqués, 1, 08028 Barcelona, Spain*

(Received 13 April 2026; revised 11 June 2026; accepted 10 July 2026; published 16 September 2026)

Nuclear density functional theory provides a unified description of finite nuclei and bulk nuclear matter, and is widely used to model the neutron star (NS) equation of state. However, extrapolations to suprasaturation densities require a quantified treatment of uncertainties arising from parameter estimation and functional choices. We present an updated Bayesian inference of a Skyrme energy density functional augmented by a flexible metamodel density dependence at high density. Nuclear observables are computed using a Gaussian emulator of the publicly available Milano HFBCS-QRPA code, enabling efficient exploration of a high-dimensional parameter space. Relative to previous analyses, we extend the calibration set with isospin-sensitive data, including masses and charge radii along selected Ca and Sn isotopic chains, and updated constraints from giant monopole resonances. The resulting posteriors are further constrained by *ab initio* neutron-matter calculations and astrophysical observations, including recent NICER measurements, yielding consistent crust and core properties of catalyzed NS compatible with current constraints. Bulk nuclear-matter parameters are well approximated by a multivariate Gaussian with covariance matrix provided for direct reuse, while several finite-nucleus parameters exhibit pronounced non-Gaussianity.

DOI: 10.1103/p6xt-x2zp

I. INTRODUCTION

Nuclear density functional theory (DFT) is among the most suitable frameworks to constrain effective nuclear interactions using laboratory data [1]. Its applicability across the nuclear chart, as well as to transport models for heavy-ion collisions and to bulk nuclear matter, makes DFT a natural tool to extrapolate phenomenological information to unknown regions of the isotope table and to density, temperature, and isospin conditions inaccessible to experiments [2,3]. For this reason, most studies of the neutron star (NS) equation of state (EoS) are carried out within the DFT framework, using relativistic (RMF) or nonrelativistic (Skyrme, Gogny) energy density functionals (EDFs) whose form and parameters are calibrated to nuclear data [4–7]; see Refs. [8,9] for a recent review. However, EDFs have limitations related to the assumed functional form governing their density dependence; in addition, they have been extensively tested in cases where experimental data allow their calibration [10–12], and the validity of current EDFs for extremely low-density or high-density neutron matter may be questioned [13]. Even in not so extreme cases, a quantified treatment of parameter-estimation uncertainties is needed for astrophysical extrapolation to regions not covered by phenomenological constraints. To address these issues, recent works [14,15] adopted a Bayesian approach to NS EoS parameter estimation. Bayesian inference yields full posterior distributions for the nucleonic EoS model parameters, whereas traditional χ^2 minimization used to construct many popular functionals provides only point estimates, typically under an implicit Gaussian approximation for uncertainties.

In Refs. [14,15], a broad set of nuclear-structure data, described with relatively simple many-body approaches such as Hartree-Fock–Bardeen-Cooper-Schrieffer (HF-BCS) and random phase approximation (RPA), was used for the inference. A full exploration of the high-dimensional parameter space was made possible by Gaussian emulators [16,17] of the nuclear-structure codes. The density dependence of the EDF was taken from the metamodel framework [18], complemented by the gradient and spin-orbit terms of the standard Skyrme functional.

*Contact author: pietro.klausner@unimi.it
†Contact author: antonelli@lpccaen.in2p3.fr
‡Contact author: gianluca.colo@mi.infn.it
§Contact author: gulminelli@lpccaen.in2p3.fr
‖Contact author: xavier.roca.maza@fqa.ub.es
¶Contact author: enrico.vigezzi@mi.infn.it

Although this meta-model extension is not as flexible as other approaches, such as Gaussian-processes EoS [19,20], or piecewise polytropes [21,22], it assures a seamless extension of the EDF to high densities for astrophysical applications. In fact, it reduces spurious correlations between low- and high-density regimes [12] induced by the restrictive Skyrme density dependence. At the same time, a mapping between the metamodel and Skyrme bulk terms at low density preserves the physical correlations between bulk and surface parameters relevant for the NS crust, enabling a consistent determination of the crustal EoS informed by nuclear-structure data.

In this paper, we present a revised and extended version of the inferences in Refs. [14,15]. The main advance is a new inference that exploits more complete information of the masses and charge radii along selected isotopic chains, providing more reliable constraints on the symmetry energy. We update the experimental input of the isoscalar giant monopole resonance (ISGMR) excitation energy based on the most recent analyses of giant monopole resonances. Finally, we propagate the resulting posterior distributions to predictions of static NS properties and incorporate the latest NICER constraints, with the goal of further restricting the high-density behavior of the EoS.

The paper is organized as follows. Section II describes the setup of our emulator-assisted inference, with emphasis on the improvements relative to the previous study in Ref. [14]. Updated results for nuclear matter and Skyrme parameters are presented in Sec. III, where we highlight the impact of the isotopic chain information on the symmetry energy parameters. Representative predictions for static NS observables are given in Sec. IV. Finally, Sec. V introduces a multivariate Gaussian approximation of our full posterior; the corresponding parameters (mean vector and covariance matrix) are reported in the Appendix for use in future analyses.

II. INFERENCE SET UP

We perform a Bayesian inference using the standard Skyrme ansatz [23] as base model and a rich pool of observables, ranging from ground state and nuclear response, as constraints. Our method follows the methodology in Ref. [14], and we refer to Sec. II therein for the details.

In Table I we show the prior distribution of the model parameters. The first ten parameters in the table are in a one-to-one correspondence with the standard Skyrme ones; see for details Refs. [24,25]. The only difference with respect to Ref. [14] is that open-shell nuclei (OS) will be now part of the observable pool. To describe the pairing correlations that emerge in OS nuclei, a standard local pairing interaction $v(\vec{r}, \vec{r}\,') = v_0\delta(\vec{r} - \vec{r}\,')$ is added in the particle-particle channel [26], and an extra parameter is added to the inference, the pairing strength v_0, considering up to six levels above the Fermi energy.

The total set of data used in the inference is presented in Table II. With respect to Ref. [14], all the observables linked to $N = Z$ nuclei have been removed. These nuclei, which are generally quite hard for EDFs to reproduce, are very sensitive to poorly known channels of the interaction such as proton-neutron pairing, that are often mocked up by the so-called Wigner term [27–29]. In the absence of such terms, the inclusion of $N = Z$ nuclei could bias the estimation of the other parameters. Therefore, to avoid adding extra parameters to our model, we simply removed these observables. We then added several ground-state properties, namely binding energies BEs [30] and charge radii $R_{\rm ch}$ [31] of open-shell isotopes of Ca and Sn. To adjust the pairing strength, we

TABLE I. Lower and upper limits of the interval of the uniform prior distribution of each model parameter.

	Units	Lower limit	Upper limit
$n_{\rm sat}$	[fm^{-3}]	0.150	0.175
$E_{\rm sat}$	[MeV]	–16.50	–15.50
$K_{\rm sat}$	[MeV]	180.00	260.00
$E_{\rm sym}$	[MeV]	24.00	40.00
$L_{\rm sym}$	[MeV]	–20.00	120.00
G_0	[MeV fm^5]	90.00	170.00
G_1	[MeV fm^5]	–90.00	70.00
W_0	[MeV fm^5]	60.00	190.00
m_0^*/m	–	0.70	1.10
m_1^*/m	–	0.60	0.90
v_0	[MeV fm^3]	150	350

TABLE II. Observables used for the inferences. The new ones are in the second part of the table, while the updated data for ^{90}Zr $E^{\rm IS}_{\rm GMR}$ is in bold font.

	Ground-state properties		
	BE [MeV]	$R_{\rm ch}$ [fm]	$\Delta E_{\rm SO}$ [MeV]
^{208}Pb	1636.4 ± 2.0	5.50 ± 0.05	2.02 ± 0.50
^{48}Ca	416.0 ± 2.0	3.48 ± 0.05	1.72 ± 0.50
^{68}Ni	590.4 ± 2.0	–	–
^{132}Sn	1102.8 ± 2.0	4.71 ± 0.05	–
^{90}Zr	783.9 ± 2.0	4.27 ± 0.05	–
	Isoscalar resonances		
	$E^{\rm IS}_{\rm GMR}$ [MeV]	$E^{\rm IS}_{\rm GQR}$ [MeV]	
^{208}Pb	13.5 ± 0.5	10.9 ± 0.5	
^{90}Zr	**18.7 ± 0.5**	–	
	Isovector properties		
	α_D [fm^3]	$m(1)$ [MeV fm^2]	$A_{\rm PV}$ (ppb)
^{208}Pb	19.60 ± 0.60	961 ± 22	550 ± 18
^{48}Ca	2.07 ± 0.22	–	2668 ± 113
	New Data from OS nuclei		
	BE [MeV]	$R_{\rm ch}$ [fm]	Δ_n [MeV]
^{50}Ca	427.5 ± 2.0	3.52 ± 0.05	–
^{46}Ca	398.8 ± 2.0	–	–
^{44}Ca	381.0 ± 2.0	–	–
^{42}Ca	361.9 ± 2.0	–	–
^{120}Sn	1020.5 ± 2.0	4.65 ± 0.05	1.3 ±0.2
^{112}Sn	953.5 ± 2.0	–	–
^{124}Sn	1050.0 ± 2.0	–	–

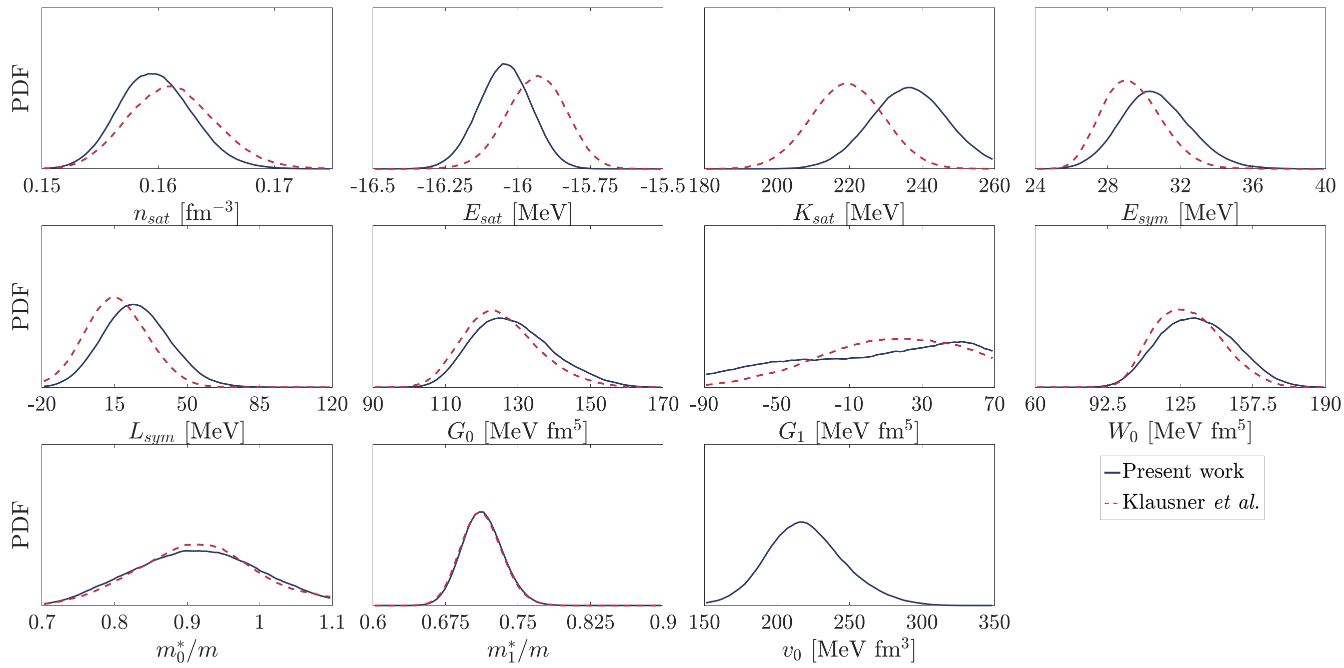

FIG. 1. Marginalized posterior distribution of the nuclear matter, surface, spin-orbit, and effective mass parameters (full blue line), compared to the previous results in Ref. [14] (dashed green line).

also included the neutron pairing gap of ^{120}Sn, obtained by the odd-even-staggering three-points mass difference formula [32], centered in the odd systems. Finally, we updated the excitation energy of the giant monopole resonance of ^{90}Zr: a newer analysis of the raw data found a higher value for the excitation energy, $E^{\mathrm{IS}}_{\mathrm{GMR}} = 18.65 \pm 0.17$ MeV [33], to be compared to the previous value $E^{\mathrm{IS}}_{\mathrm{GMR}} = 17.66 \pm 0.07$ MeV [34]. As we demonstrate in the next section, the primary effect of a larger excitation energy $E^{\mathrm{IS}}_{\mathrm{GMR}}$ is to shift the distribution of K_{sat} and n_{sat}; cf. Fig. 5 of Ref. [14]. Concerning the other observables, we refer to Ref. [14] for their description and associated references.

For all observables, the uncertainties quoted in Table II that will enter the likelihood (a product of uncorrelated Gaussian functions) of the Bayesian inference comprise both the experimental uncertainty and the theoretical uncertainty associated to the DFT description. The latter is the dominant source of uncertainty for all observables except the isovector properties. For these observables, we employed directly the experimental error, which is large. The theoretical errors were chosen to reflect the fact that standard EDFs usually describe binding energies and charge radii within a few MeV and a few 10^{-2} fm, respectively, rather than within the much smaller experimental uncertainties. While dedicated mass models can describe binding energies across the nuclear chart with a root-mean-square error of about 0.5 MeV, we adopt broader values, namely 2 MeV for binding energies and 0.05 fm for charge radii, which are typical uncertainty scales for standard EDFs with a limited number of parameters. These choices should therefore be understood as effective global model-discrepancy scales (i.e., they set the level of accuracy that we demand from the EDF in the present global calibration) and do not provide an explicit treatment of correlations among theoretical residuals, which would require a dedicated covariance discrepancy model (see, e.g., Ref. [35]).

To allow the full exploration of the parameter space within acceptable computation time limits, we use the Gaussian emulator [16], developed by the MADAI Collaboration [17], to emulate the behavior of the HFBCS-QRPA code [36,37]. For technical details about the Bayesian inference and the validation of the emulator we refer to Ref. [14].

III. INFERENCE RESULTS: NUCLEAR STRUCTURE DATA

In Fig. 1, we show the marginalized posterior distribution of the parameters, comparing the new results (full line) with those of Ref. [14] (dashed line). The surface parameter G_0 and G_1, the spin-orbit parameter W_0 and the two effective masses are only slightly affected by the new data. K_{sat} is increased as an effect of the new ^{90}Zr monopole excitation energy and n_{sat} is lowered as it is anticorrelated to K_{sat}. Instead, the new calcium and tin isotopes, together with the removal of $N = Z$ nuclei, shift the E_{sat} distribution to lower values. In general, as we observed in Ref. [14], to which we refer for more details, our findings for these parameters are in line with previous studies [38–41]. Although both E_{sym} and L_{sym} are shifted to higher values, however by a rather modest amount, their values are relatively low with respect to other works in the literature [8,9,42]. Though we already pointed out this feature in our previous analysis [14], we now observe that values of $L_{\mathrm{sym}} > 50$ MeV are less disfavored by the inclusion of open-shell nuclei than before, and are not outright excluded anymore. This makes our findings more in line with those of previous studies (see, e.g., Refs. [10,11]).

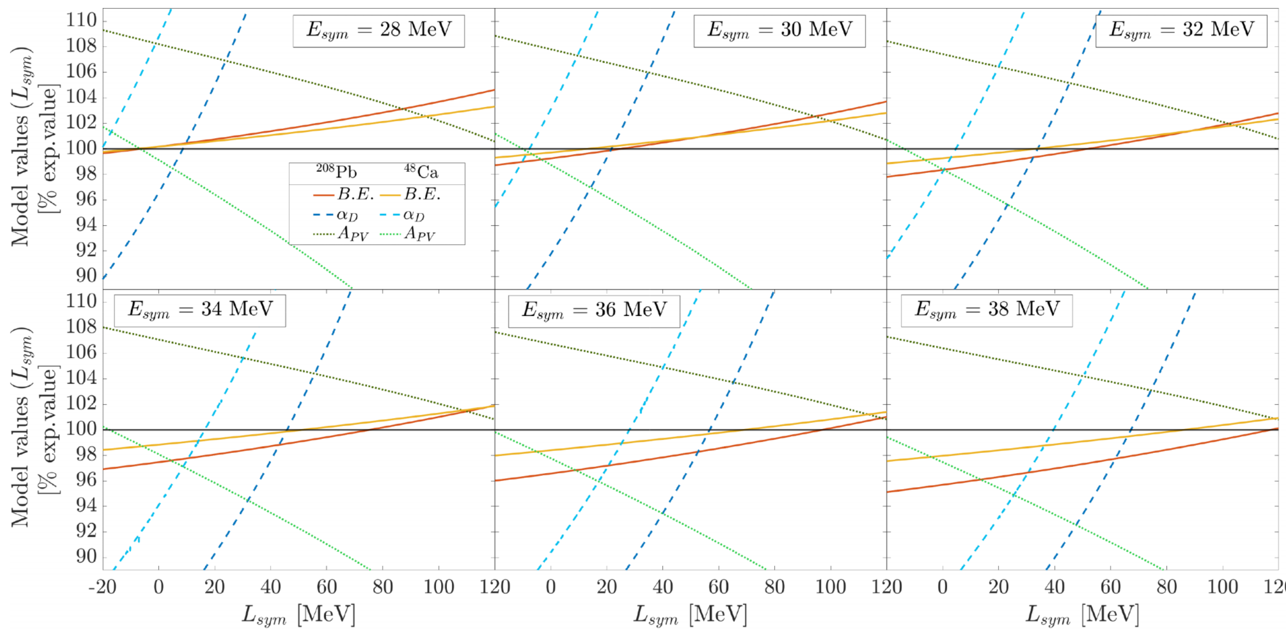

(a)

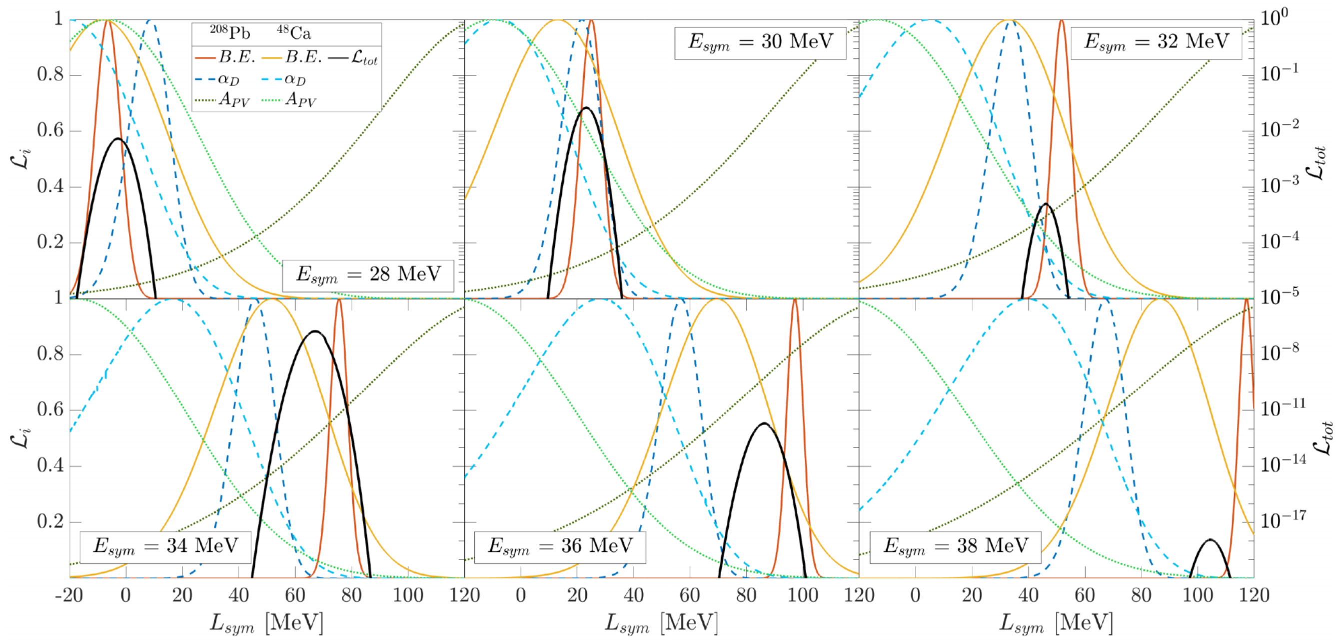

(b)

FIG. 2. Model results, likelihoods $\mathcal{L}_i$ associated with selected observables in ^{48}Ca and ^{208}Pb and total likelihood $\mathcal{L}_{\text{tot}}$ as a function of L_{sym}. E_{sym} it has been fixed to six values, from 28 to 38 MeV in steps of 2 MeV, while all the other parameters have been fixed at the best likelihood model of the complete inference. (a) Model results as a function of L_{sym}. (b) Likelihood $\mathcal{L}$ as a function of L_{sym}.

To investigate this persisting softness of the symmetry energy, we performed a sensitivity study, probing the dependence of some selected observables in ^{48}Ca and ^{208}Pb on L_{sym}, fixing all the parameters to their best $\log(\mathcal{L})$ value, except for E_{sym}, which we varied from 28 MeV to 38 MeV, in steps of 2 MeV, and of course L_{sym}, which remained free. In Fig. 2(a) we show the HFBCS-QRPA code results as a function of L_{sym}. On the x axis we have the full prior interval of L_{sym}, while on the y axis the theoretical result of the HFBCS-QRPA code for selected binding energies and for the isovector observables of ^{48}Ca and ^{208}Pb, expressed as a percentage of the experimental value. 100%, perfect accordance with the experiment, is highlighted with a black horizontal line. The orange lines are the BEs of the representative nuclei ^{208}Pb (darker) and ^{48}Ca (lighter). We can observe the expected correlation induced on $E_{\text{sym}} - L_{\text{sym}}$: with increasing E_{sym}, a higher value of L_{sym} is needed to match

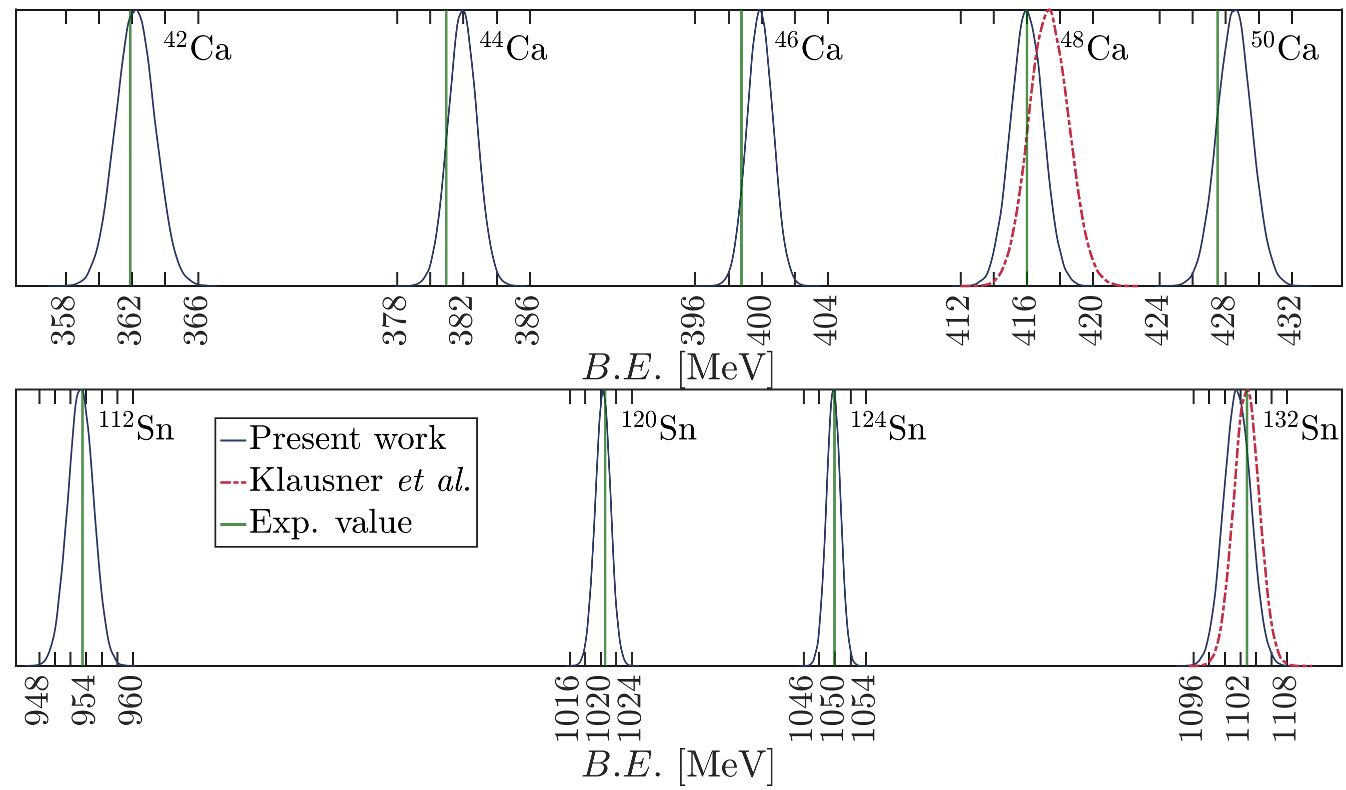

FIG. 3. Binding energy posterior distribution for the Ca and Sn isotopic chains (full blue line), compared to the results of Klausner *et al.* [14] (dashed green line). The red vertical line marks the experimental value.

the experimental result. Overall, the BEs vary by about 5% of the experimental value over the L_{sym} range.

The dashed lines represent the polarizability α_D of ^{208}Pb (dark blue) and ^{48}Ca (light blue), while the dotted ones are the parity-violating asymmetries A_{PV} of ^{208}Pb (dark green) and ^{48}Ca (light green). As expected from previous works [43], A_{PV} decreases as L_{sym} grows, while the polarizabilities grow with L_{sym} [44,45]. A_{PV} changes rather slowly, spanning $\approx$ 10–15% of the experimental value across the L_{sym} prior interval, while α_D has a quite steep gradient, varying significantly in an interval of $\approx$40 MeV. If we look at the observables uncertainties in Table II, we see that, while A_{PV} and α_D have a relative error of $\approx$3% ($\approx$10% ^{48}Ca), the BEs impose a much tighter constraint, as they have an error of some parts per thousand. This brings us to the main argument: the posterior will be non-negligible only in zones where the model prediction for the BEs is close to the experimental value. In $E_{\text{sym}} - L_{\text{sym}}$ terms, it means that it follows the correlation imposed by the masses. On that correlation, the optimal solutions can either land on high $E_{\text{sym}} - L_{\text{sym}}$ zones, where one can describe fairly well the BEs together with the ^{208}Pb A_{PV}, or on low $E_{\text{sym}} - L_{\text{sym}}$ regions, where one can describe the BEs and α_D simultaneously. Since α_D has a much steeper dependence on L_{sym} than A_{PV}, and their relative error is similar, the associated likelihood $\mathcal{L}_{\alpha_D}$ will fall off much more rapidly than $\mathcal{L}_{A_{\text{PV}}}$ when moving away from the regions where the model reproduces the experimental results.

This becomes even clearer if we look directly at the likelihood $\mathcal{L}_i$ for each observable. Figure 2(b) is the same as 2(a), but instead of showing the model results as a function of L_{sym}, it shows directly the $\mathcal{L}_i$ relative to each observable. The thick black line is the total likelihood $\mathcal{L}_{\text{tot}}$, i.e., the product of the single likelihoods of the selected observables. We see that for $E_{\text{sym}} = 30$ MeV $\log(\mathcal{L}_{\text{tot}})$ reaches its highest value; at $E_{\text{sym}} = 28$ MeV its peak decreases by approximately 70%. For $E_{\text{sym}} \geqslant 32$ MeV, $\mathcal{L}_{\text{tot}}$ plummets: in the bottom row, where we had to change the scale, we can observe it is several orders of magnitude lower than at $E_{\text{sym}} = 30$ MeV. Therefore, the reason we find relatively low values of E_{sym} and L_{sym} with respect to other works in the literature [8,9,42] lies in the request of simultaneously describing the polarizabilities and the binding energies within the corresponding uncertainties.

Given the notable effect BEs can have on the $E_{\text{sym}} - L_{\text{sym}}$ distributions, adding open-shell isotopes of tin and calcium lowers the risk of a singular BE biasing the final results. However, the arguments we presented in Fig. 2 still hold, thus explaining the low values of $E_{\text{sym}} - L_{\text{sym}}$ we again find in this work. We can see that a careful choice of the theoretical errors is fundamental to obtain a reliable estimation of the parameters. Imposing larger uncertainties to the masses would have resulted in different predictions for the NMP of the isovector sector. The uncertainties here considered are consistent with the predictive value of the model, as it can be *a posteriori* verified looking at the posterior distribution of BEs.

To this aim, we extracted 10^5 samples from the posterior distribution. As an example, we display in Fig. 3 the binding energy posteriors for the Ca and Sn isotopic chains: with the addition of the OS data, we observe a clear improve-

TABLE III. Standard deviations σ, in MeV, of the posterior distribution of BE in Fig. 3.

	^{42}Ca	^{44}Ca	^{46}Ca	^{48}Ca	^{50}Ca	^{112}Sn	^{120}Sn	^{124}Sn	^{132}Sn
σ	1.16	0.86	0.77	0.97	1.03	1.63	1.00	0.91	1.74

ment of the description of ^{48}Ca, at the price of only a slight worsening of that of ^{132}Sn. Given that these distributions are well behaved and single peaked, we estimate their width with their standard deviation, which are all in the order of the MeV, as shown in Table III. Therefore, our initial guess of theoretical error (2 MeV) is in line with the predictive power of the model.

We also computed the posterior distribution of binding energies and charge radii of 150 known spherical nuclides along the nuclear chart. We show the results in Fig. 4. The squares relative to different species are colored by the distance $|\Delta_{\mathrm{BE}}|$ ($|\Delta_{R_{\mathrm{ch}}}|$) between the mean of our posterior and the experimental value: green if the distance is less than 2 MeV or 0.05 fm, which are the theoretical errors we assumed (see Table II); orange if it is between 2 and 4 MeV or between 0.05 and 0.1 fm; and finally red if it is more than 4 MeV or 0.1 fm. As we can observe, for the BEs the vast majority is colored in green (91%); the rest is mostly orange (8%), with only one instance of red. For the R_{ch}, all are green except for two red instances. As an overall measure of performance, the root-mean-square (RMS) is 1.23 MeV for binding energies and 0.02 fm for charge radii, while the mean distance from experimental values is 0.97 MeV for binding energies and 0.02 fm for charge radii.

Concerning the isovector-sensitive observables, all posteriors are compatible with the experimental results, except for the ^{208}Pb A_{PV}, in agreement with the results of Ref. [14]. The tension between PREX-II data and the other isovector-sensitive observables is shown in Fig. 5, where we plot the corner plot of the α_D and A_{PV} posteriors. From the marginalized distributions shown in the diagonal plots we can see that ^{208}Pb α_D is well reproduced by our inference, while ^{48}Ca α_D and ^{48}Ca A_{PV} are slightly over- and underestimated, but still with significant overlap with the experimental error. On the other hand, looking at the correlation plots, it is clear that the model cannot reproduce simultaneously ^{208}Pb A_{PV} and the other isovector-sensitive observables, corroborating other analyses, which highlighted this tension.

The apparent incompatibility of ^{208}Pb A_{PV} with the other observables might hint to the need of improving our EDF, that would be important for the description of this specific observable. For example, it was recently suggested [46–48] that a strong isovector spin-orbit interaction could reconcile the CREX and PREX-II experiments, although following studies hinted that this idea might not be the correct solution to the PREX-CREX puzzle [49]. Other strategies, with updated EDF with additional term, were presented in Refs. [50,51]. It would be worth, on the other hand, to measure again the A_{PV} at other facilities and/or with a different kinematics.

The difficulty of reproducing ^{208}Pb A_{PV} within our theoretical framework naturally leads to question whether the inclusion of this data point in the inference could not lead to biased results. To answer this question, we have checked that no significant difference is observed in the nuclear matter parameter posteriors when the inference is repeated omitting the ^{208}Pb A_{PV} from our pool of data. Hence, on the basis of the

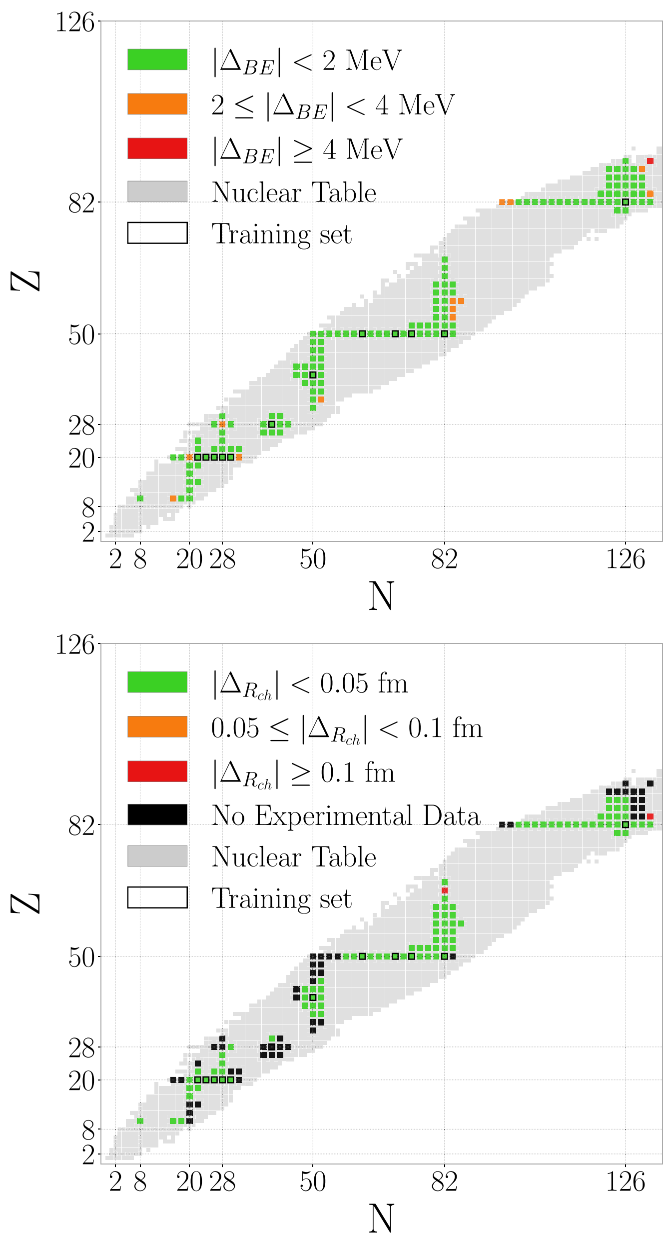

FIG. 4. Performance over the nuclear chart (gray squares) of the posterior distribution, for the BEs of 150 spherical nuclei and R_{ch}. The squares relative to different species are colored by the distance $|\Delta_{\mathrm{BE}}|$ ($|\Delta_{R_{\mathrm{ch}}}|$) between the mean of our posterior and the experimental value: green if the deviation is less than 2 MeV or 0.05 fm; orange if it is between 2 and 4 MeV or between 0.05 and 0.1 fm; and finally red if it is more than 4 MeV or 0.1 fm. The nuclei used in the training set (Table II) are contoured by a black line.

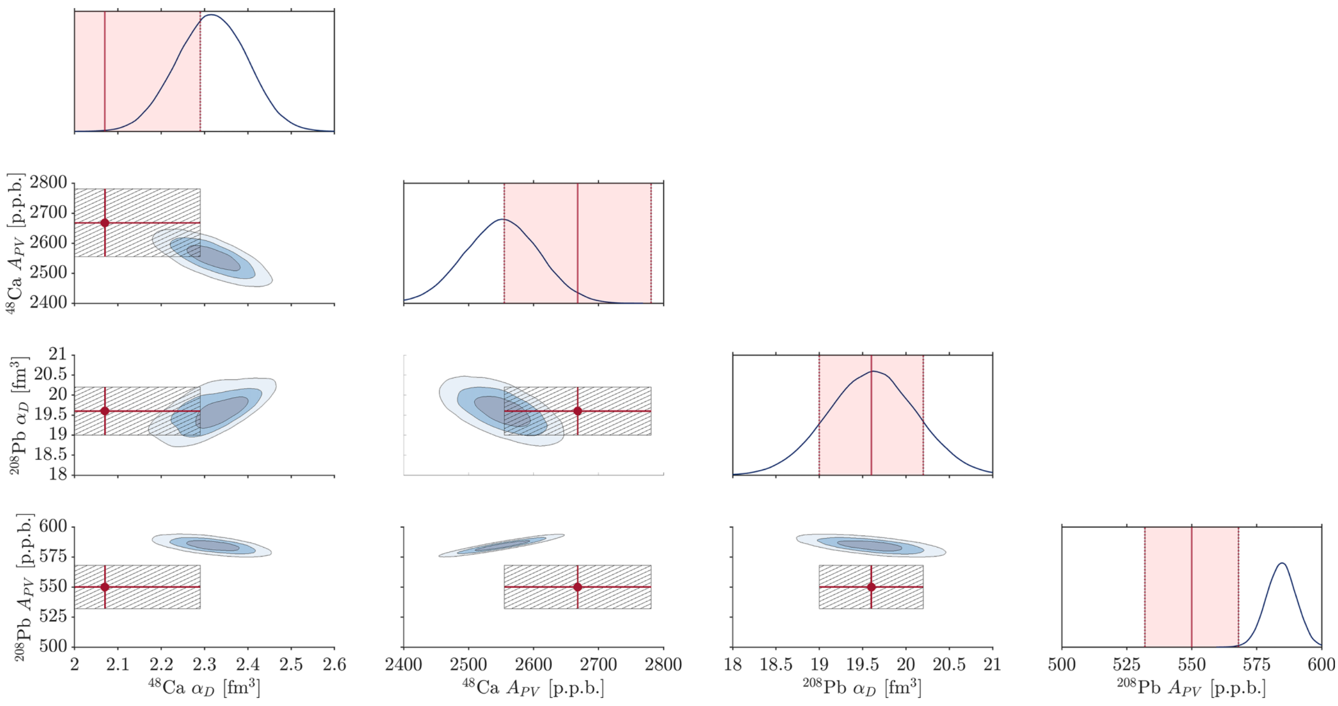

FIG. 5. Corner plot for the α_D and A_{PV} posterior distribution of ^{208}Pb and ^{48}Ca. The red vertical lines in the diagonal plots mark the experimental value, while the red shaded areas show the 1σ region. The rectangular hatched regions of the off-diagonal plots corresponds to the 1σ uncertainty of both experiments, with the red dot indicating the experimental results.

used EDF, the incompatibility of the ^{208}Pb A_{PV} with the other observables in the data pool is not statistically significant.

IV. INFERENCE RESULTS: ASTROPHYSICAL DATA

We now turn to the implications of our results for NS physics. For this analysis, we follow the procedure outlined in Ref. [15], to which we refer for details.

We use the full posterior distribution obtained in Sec. III as the prior for a subsequent Bayesian inference that includes χ-EFT calculations of pure neutron matter (from 0.02 fm^{-3} to 0.2 fm^{-3}) and astrophysical constraints: maximum pulsar masses, tidal polarizability from GW170817, and four independent NICER measurements; see Refs. [15,52] for a precise definition of the associated Bayesian likelihoods. A recent reanalysis suggests a lower mass for the pulsar J0348 + 0432 (i.e., $1.806 \pm 0.037\,M_\odot$, see Ref. [53]) than the previously inferred value of $2.01 \pm 0.04\,M_\odot$ [54]. Relative to Ref. [15], we therefore replace the previous maximum observed NS mass constraint from Ref. [54] with the $2.08 \pm 0.07\,M_\odot$ mass of pulsar J0740 + 6620 inferred from Shapiro delay measurements [55]. Concerning the other astrophysical and stability-causality constraints, we refer to Refs. [15,52] for details.

Using the nuclear posterior from Sec. III as the prior for the astrophysical update has two advantages. First, it propagates all the correlations among nuclear matter parameters implied by our emulator-assisted calibration. Second, it ensures that all parameter sets retained by the combined astrophysics+laboratory inference remain consistent with the nuclear observables used in the first stage fit. In particular, because bulk and surface terms are inferred jointly in the first stage fit of Sec. III, each parameter set uniquely defines a unified crust-core EoS: the same EDF determines homogeneous matter in the core and all the relevant crust properties, which are computed with the semiclassical extended Thomas-Fermi approach as in Ref. [15]. In our hybrid Skyrme+metamodel inference, the nuclear and astrophysical constraints are combined sequentially via factorized likelihoods: finite-nucleus observables constrain the Skyrme sector, and the resulting multidimensional posterior is propagated to the neutron star inference through the Skyrme-derived interface used by the metamodel. This interface includes the low-order NMPs sampled in the Skyrme sector of the inference (see Table I) and derived quantities such as $K_{\mathrm{sym}}^{\mathrm{Sk}}$, which is not independently sampled (see Ref. [15] for details). The metamodel is then used to provide the additional high-density freedom required for neutron star matter. Therefore the procedure is not an attempt to reproduce a pure Skyrme extrapolation at high density, nor a claim of equivalence with an unavailable fully unified inference, where the same nuclear model is used for both finite nuclei and neutron star matter. It is a controlled inference protocol that preserves the nuclear information relevant for the low-density and crust sectors while avoiding the spurious high-density rigidity of the Skyrme functional. Moreover, our protocol is expected to retain most of the posterior correlations among the low-order NMPs, as they are directly informed by both astrophysical and nuclear data.

The more detailed information on the symmetry sector of the EoS provided by the inclusion of Ca and Sn isotopic chains

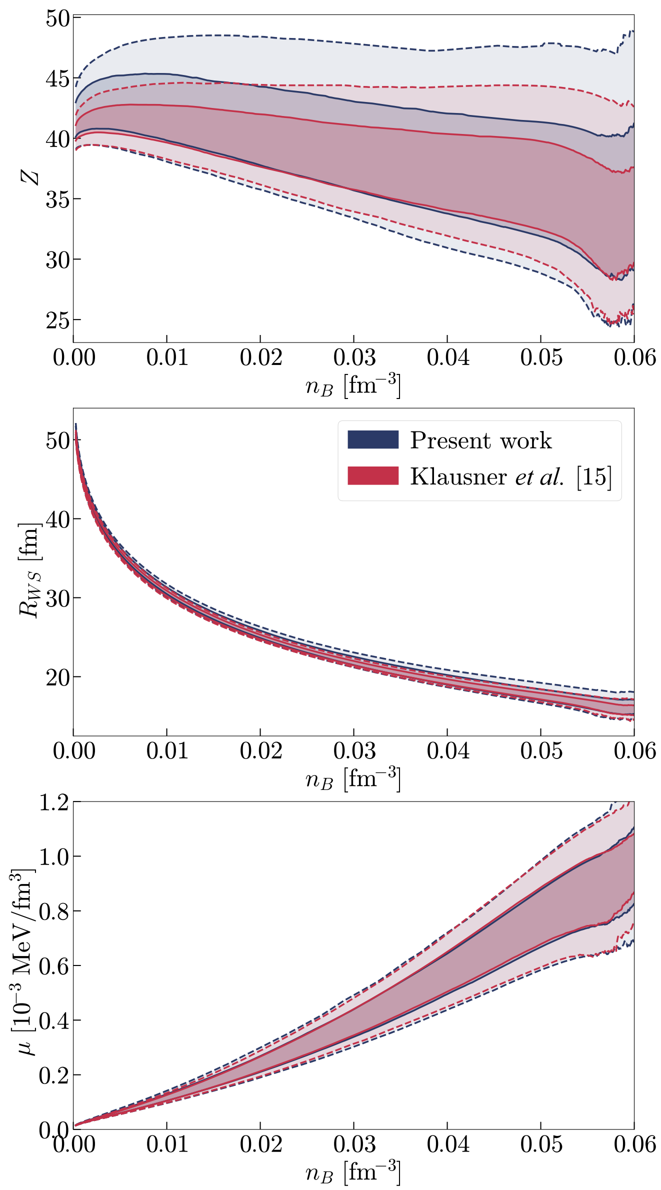

FIG. 6. Posterior distributions of selected crust properties (proton number in the Wigner-Seitz cell Z, cell radius R_{WS}, and shear modulus μ) for the two inferences: this work (light blue) and the previous results in Ref. [15] (light green). Darker shaded regions show the 68% credible interval, and lighter shaded regions the 95% credible interval.

has a sizable influence on the crust composition, as can be seen from the top panel of Fig. 6, which shows the posterior distribution of the ion charge Z as a function of the baryon density in the crust. The higher value of the symmetry energy at low density compared to the results of Ref. [14] leads to systematically higher ion charges. This is in qualitative agreement with the microscopic calculations of Ref. [56], where lower symmetry energies were shown to yield lower proton fractions in the crust, based on HFB calculations with four selected BSK functionals (see also Ref. [57]).

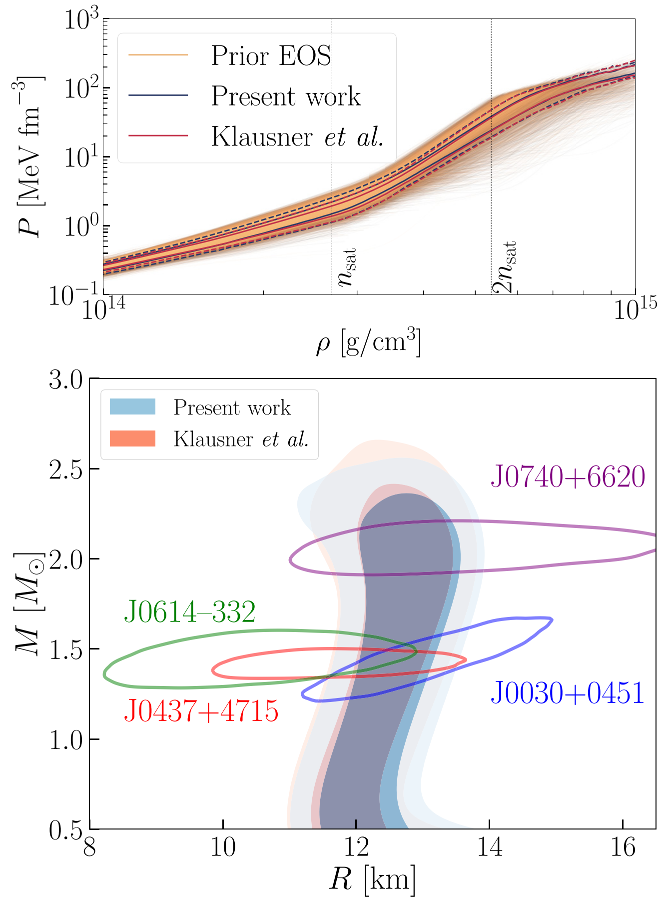

FIG. 7. Posterior of the neutron star EoS (top part) and of the mass-radius relation (bottom part) for the two inferences: this work in blue, and our previous results [14] in red. In the top panel, the straight line encloses the 68% CI region, while the dotted the 95%; in the bottom, the darkest region encloses the 68% CI region, while the lighter the 95%. The four colored contours in the bottom panel encircle the 95% probability region of the four NICER measurements [61–64]. For the top plot, we also plotted in orange prior samples of the neutron star EoS satisfying the chiral constraint.

On the other hand, the improved estimation of the nuclear matter parameters does not have a sizable influence on the global properties of the Wigner-Seitz cell, such as the central and gas density (not shown) or the Wigner-Seitz radius, shown in the central panel of Fig. 6. The same is true for the thermodynamic properties of the crust. This includes the crustal pressure (see Fig. 7 below) and the shear modulus, displayed in the bottom panel of Fig. 6. This latter is important to estimate dynamic properties of the crust, such as torsional oscillations and interface modes, see, e.g., Ref. [58]. Taking into account the effect of the ion finite size, the shear modulus can be approximated as [59]:

$$\mu = 0.1194 \frac{3(Ze)^2}{4\pi R_{WS}^4}\left(1 - \frac{u^{5/3}}{2 - 4u^{1/3} + 3u}\right), \tag{1}$$

u being the cluster volume fraction, see also Ref. [60]. From Fig. 6 we can see that the modification of the ion charge has a negligible impact on the estimation of the shear modulus.

The influence of the additional information provided by the open-shell nuclei is also very weak in the determination of the global stellar properties. This is demonstrated by Fig. 7, where we show the EoS (pressure P vs mass density ρ) and mass-radius posteriors relation of our results in comparison to those of Klausner *et al.* [14]. For the EoS, we also show, in various degree of orange, the EoS of prior samples satisfying the chiral constraint. Their β-equilibrated NS EoS is stable (no pressure drop with increasing density) and causal (speed of sound not exceeding that of light).

As expected, the two results are very similar, and are well compatible with NICER measurements. The main difference between this work and the results presented in Ref. [15] concern the nuclear data selected for the analysis, and particularly the revised value of the giant monopole resonance and the inclusion of the mass and radius information of ^{42,44,46,48,50}Ca and ^{112,120,124,132}Sn isotopes. As we have seen in Sec. III, this experimental information only affects the low-order nuclear matter parameters $E_{\rm sat}$, $K_{\rm sat}$, $E_{\rm sym}$, $L_{\rm sym}$. Consistently, the only visible differences of the two analyses concern the low-density region of the EoS and the behavior of the mass-radius correlation for masses below $\approx 1M_\odot$. The stiffening of the EoS induced by the more complete nuclear physics information of the present work leads to a slight increase of the NS radius for extremely low masses, which however are not expected to be produced in the stellar evolution.

In particular, the slope changes in the EoS between one- and two-times saturation densities, already observed in Ref. [15], is still present in this new version of the analysis. Indeed the nuclear structure information suggests a very soft EoS especially in the isovector sector. The 2 $M_\odot$ maximum mass requirement therefore demands an important stiffening of the EoS at densities above the ones explored by nuclear structure experiments, and this stiffening is moderated at high density by the gravitational wave GW170817 information.

Finally, we summarize in Table IV other properties of NSs for the two representative masses $M = 1.4,\ 2\,M_\odot$: their radius R, their crustal radius R_c, the adimensional tidal deformability Λ, and the density n_{cc} and pressure P_{cc} at the crust-core transition. It is worth noting that we do not find the bimodality feature of the $R_{1.4}$ posterior distribution, as was reported in Ref. [66]; rather, our posterior is single-peaked at approximately 12.5 km, and decays to effectively 0 below 11.5 km and above 13.5 km.

V. GAUSSIAN APPROXIMATION OF NUCLEAR POSTERIOR

The nuclear posterior distribution of Fig. 1, containing a large amount of available information from nuclear structure data, can be used as a nuclear informed prior for more advanced astrophysical analyses than the simple applications shown in the present paper. It can also be used for the generation of representative EoS models complying with nuclear

TABLE IV. Median value and 68% confidence interval limits of the star radius R, the crust radius R_c, the adimensional tidal deformability Λ, for 1.4 and 2.0 $M_\odot$ NSs, and the density n and pressure P of the crust-core transition. All these quantities are computed from the nuclear priors described above.

		$M[M\odot]$	Present Work	Klausner *et al.* [14]
R	[km]	2.0	$12.9^{+0.4}_{-0.4}$	$12.9^{+0.3}_{-0.3}$
		1.4	$12.6^{+0.3}_{-0.3}$	$12.5^{+0.3}_{-0.3}$
R_c	[km]	2.0	$0.71^{+0.07}_{-0.07}$	$0.71^{+0.06}_{-0.06}$
		1.4	$1.16^{+0.09}_{-0.08}$	$1.14^{+0.07}_{-0.08}$
Λ		2.0	$68.5^{+18.8}_{-15.2}$	$67.4^{+16.5}_{-11.9}$
		1.4	$557.6^{+98.5}_{-75.2}$	$544.8^{+83.1}_{-69.1}$
$n_{\rm cc}$	[fm^{-3}]	–	$0.090^{+0.008}_{-0.007}$	$0.092^{+0.011}_{-0.009}$
$P_{\rm cc}$	[MeV fm^{-3}]	–	$0.52^{+0.07}_{-0.08}$	$0.52^{+0.08}_{-0.08}$

physics constraints, to be used in dedicated astrophysical simulations.

For these future applications, an analytical approximation of the posterior might be useful. The distributions in Fig. 1 are bell shaped, except for the parameter G_1. Therefore, a good analytical representation of this posterior is given by a multivariate Gaussian:

$$\mathcal{N}(\mathbf{x}|\boldsymbol{\mu},\boldsymbol{\Sigma}) \propto \exp\left(-\frac{1}{2}(\mathbf{x}-\boldsymbol{\mu})^{\rm T}\boldsymbol{\Sigma}^{-1}(\mathbf{x}-\boldsymbol{\mu})\right), \qquad (2)$$

where $\boldsymbol{\mu}$ is the mean vector and $\boldsymbol{\Sigma}$ is the covariance matrix (both can be easily obtained from our posterior sample and are given in the Appendix). Figures 8 and 9 compare the full posterior obtained via our sampling procedure with its analytical approximation $\mathcal{N}(\mathbf{x}|\boldsymbol{\mu},\boldsymbol{\Sigma})$. Apart from G_1, whose bimodal behavior cannot be captured by a single multivalued Gaussian, the remaining parameters are well reproduced.

Regarding Fig. 8, it is important to stress that in standard Skyrme interactions the higher-order nuclear-matter parameters $Q_{\rm sat}$, $Z_{\rm sat}$, $K_{\rm sym}$, $Q_{\rm sym}$, and $Z_{\rm sym}$ are constrained by the lower-order ones [12]. For meaningful astrophysical applications, these parameters should not be treated as independent degrees of freedom above saturation, as discussed in Ref. [15]. However, they may be needed for some applications concerning the subsaturation EoS, like for studying crust properties. Therefore, for completeness, we include their distribution in our multivariate Gaussian. The optimal values of $\boldsymbol{\mu}$ and $\boldsymbol{\Sigma}$ are listed in the Appendix, see Tables V and VI, and are also available in the Supplemental Material [65] in a more convenient format.

VI. CONCLUSIONS

Using a Gaussian emulator of the publicly available Milano HFBCS-QRPA code [36,37] for nuclear structure calculations, we have performed a Bayesian analysis of a large set of EoS-sensitive static and dynamic observables, including both closed-shell and open-shell nuclei. A standard Skyrme interaction augmented with a more flexible density dependence at supersaturation density is employed. The posterior 16-dimensional distribution of the associated bulk and surface

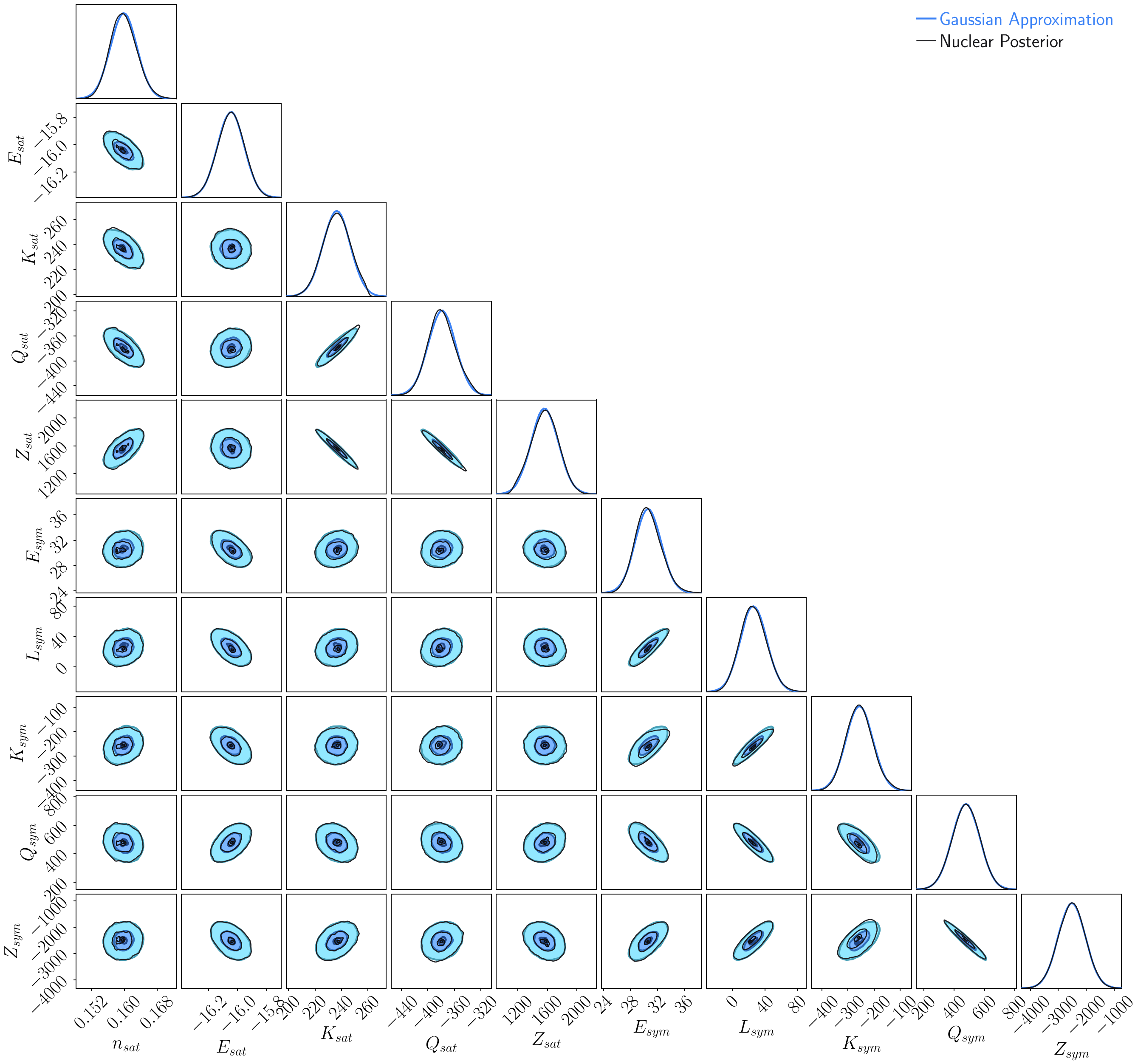

FIG. 8. Gaussian approximation of the nuclear posterior. Focus: nuclear matter parameters.

parameters is used in a second Bayesian inference to include constraints from *ab initio* neutron matter calculations and astrophysical observations. This allows a consistent calculation of crustal as well as core properties of catalyzed neutron stars, which is in agreement with present observations. The posterior distribution of bulk parameters can be accurately fitted by a multivariate Gaussian, whose parameters are given for future applications. Concerning the parameters characteristic of finite nuclei (surface, spin-orbit, and pairing), their complex distribution shows considerable deviations from a Gaussian behavior, and numerical values are available upon request to the authors.

This work is a follow up of similar previous analyses [14,15]. With respect to these works, we have increased the pool of isospin-sensitive observables by extending the analysis to open-shell nuclei with the inclusion of an extra pairing parameter. The extra information brought by the inclusion of Ca and Sn isotopic chains leads to a sizable modification of the low-order nuclear matter parameters in comparison to Ref. [14], and an improved description of the neutron star crust.

Possible extensions of the present work include applying the same inference protocol to different EDF families, such as RMF models, or to more flexible nonrelativistic functionals, such as the KIDS [67–69] or Fayans functionals [70], which could provide additional freedom in the isovector sector (see Ref. [12]). A systematic comparison of posterior distributions obtained with different functionals, but with the same statistical protocol and the same calibration data, would help quantify the model dependence of the inferred nuclear-matter and neutron star properties. A complementary issue concerns the choice of nuclear observables entering the likelihood. As discussed above, both the selected dataset and the adopted theoretical uncertainties can have a significant impact on the posterior distributions. It would therefore be useful to investigate which minimal set of nuclear observables is most effective in constraining the behavior of nuclear matter, which uncertainties should be assigned to the different classes of observables, and which measurements should be excluded. Such studies would help establish more robust protocols for future Bayesian EDF calibrations and would make comparisons among different statistical analyses less ambiguous.

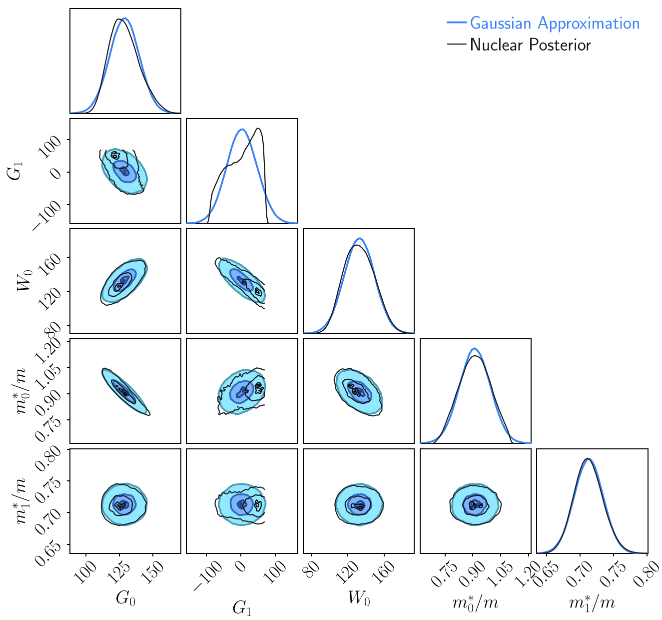

FIG. 9. Gaussian approximation of the nuclear posterior. Focus: surface parameters.

ACKNOWLEDGMENTS

This work has been partially supported by the IN2P3 Master Project MAC. X.R.M. acknowledges support by MI-CIU/AEI/10.13039/501100011033 and by FEDER UE through grants PID2023-147112NB-C22; and through the "Unit of Excellence Maria de Maeztu 2025–2028" award to the Institute of Cosmos Sciences, grant CEX2024-001451-M. Additional support is provided by the Generalitat de Catalunya (AGAUR) through Grant No. 2021SGR01095.

DATA AVAILABILITY

The data that support the findings of this article are not publicly available upon publication because it is not technically feasible and/or the cost of preparing, depositing, and hosting the data would be prohibitive within the terms of this research project. The data are available from the authors upon reasonable request.

APPENDIX: MEAN VECTOR AND COVARIANCE MATRIX

We approximate the posterior sample of EDF parameters (or derived nuclear-matter parameters) with a single multivariate normal distribution $\mathcal{N}(\mathbf{x}|\boldsymbol{\mu}, \boldsymbol{\Sigma})$ by matching the posterior's sample mean and covariance, see Eq. (2). This provides a compact representation of the full posterior that allows downstream users to propagate uncertainties using only $\boldsymbol{\mu}$ and $\boldsymbol{\Sigma}$. This compression of the full posterior information into $\boldsymbol{\mu}$ and $\boldsymbol{\Sigma}$ reproduces linear correlations extremely well, but it does not capture possible skewness or multimodality features, most notably for G_1 (the quality of this compression is illustrated in Figs. 8 and 9).

The mean vector $\boldsymbol{\mu}$ and of the (symmetric and positive-definite) covariance matrix $\boldsymbol{\Sigma}$ are given in Tables V and VI.

TABLE V. Mean values $\boldsymbol{\mu}$ for the 15 variables $\mathbf{x}$ in our posterior. The marginal distribution of each x_i ($i = 1, \dots, 15$) is an univariate Gaussian with standard deviation $\sigma_i = \sqrt{\Sigma_{ii}}$, which is also reported.

	$\mathbf{x}$	μ_i	σ_i	
1	n_{sat}	1.6×10^{-1}	3.2×10^{-3}	fm^{-3}
2	E_{sat}	-1.6×10^{1}	9.1×10^{-2}	MeV
3	K_{sat}	2.4×10^{2}	1.0×10^{1}	MeV
4	Q_{sat}	-3.8×10^{2}	2.0×10^{1}	MeV
5	Z_{sat}	1.6×10^{3}	1.8×10^{2}	MeV
6	E_{sym}	3.1×10^{1}	1.9	MeV
7	L_{sym}	2.6×10^{1}	1.6×10^{1}	MeV
8	K_{sym}	-2.6×10^{2}	5.1×10^{1}	MeV
9	Q_{sym}	4.8×10^{2}	8.9×10^{1}	MeV
10	Z_{sym}	-2.5×10^{3}	4.8×10^{2}	MeV
11	m_0^*/m	9.1×10^{-1}	8.3×10^{-2}	–
12	m_1^*/m	7.1×10^{-1}	2.1×10^{-2}	–
13	G_0	1.3×10^{2}	1.1×10^{1}	MeV fm^5
14	G_1	2.8	4.4×10^{1}	MeV fm^5
15	W_0	1.3×10^{2}	1.7×10^{1}	MeV fm^5

TABLE VI. Covariance matrix $\mathbf{\Sigma}$ for the 15 variables $\mathbf{x}$ listed in Table V.

Σ_{ij}	1	2	3	4	5
1	1.0×10^{-5}	-1.8×10^{-4}	-1.8×10^{-2}	-4.2×10^{-2}	3.8×10^{-1}
2	-1.8×10^{-4}	8.2×10^{-3}	-4.1×10^{-2}	2.9×10^{-1}	-2.1
3	-1.8×10^{-2}	-4.1×10^{-2}	1.0×10^{2}	1.9×10^{2}	-1.8×10^{3}
4	-4.2×10^{-2}	2.9×10^{-1}	1.9×10^{2}	4.1×10^{2}	-3.6×10^{3}
5	3.8×10^{-1}	-2.1	-1.8×10^{3}	-3.6×10^{3}	3.3×10^{4}
6	6.1×10^{-4}	-9.5×10^{-2}	2.9	3.1	-2.4×10^{1}
7	8.5×10^{-3}	-8.2×10^{-1}	2.9×10^{1}	4.3×10^{1}	-2.9×10^{2}
8	3.7×10^{-2}	-2.3	2.2×10^{1}	9.6×10^{1}	1.7×10^{1}
9	-3.8×10^{-2}	4.0	-2.6×10^{2}	-2.6×10^{2}	3.1×10^{3}
10	9.6×10^{-2}	-1.9×10^{1}	1.8×10^{3}	1.8×10^{3}	-2.3×10^{4}
11	-3.0×10^{-6}	8.9×10^{-4}	1.1×10^{-2}	-3.9×10^{-1}	5.6×10^{-1}
12	4.6×10^{-7}	-9.8×10^{-6}	-6.5×10^{-4}	-2.3×10^{-3}	1.6×10^{-2}
13	9.6×10^{-4}	-2.3×10^{-1}	-1.5×10^{1}	1.8×10^{1}	2.1×10^{2}
14	-2.3×10^{-2}	6.1×10^{-1}	2.3×10^{1}	6.7	-4.7×10^{2}
15	-4.7×10^{-3}	1.0×10^{-1}	-9.0	3.2×10^{1}	1.7×10^{1}

Σ_{ij}	6	7	8	9	10
1	6.1×10^{-4}	8.5×10^{-3}	3.7×10^{-2}	-3.8×10^{-2}	9.6×10^{-2}
2	-9.5×10^{-2}	-8.2×10^{-1}	-2.3	4.0	-1.9×10^{1}
3	2.9	2.9×10^{1}	2.2×10^{1}	-2.6×10^{2}	1.8×10^{3}
4	3.1	4.3×10^{1}	9.6×10^{1}	-2.6×10^{2}	1.8×10^{3}
5	-2.4×10^{1}	-2.9×10^{2}	1.7×10^{1}	3.1×10^{3}	-2.3×10^{4}
6	3.6	2.7×10^{1}	6.7×10^{1}	-1.2×10^{2}	5.8×10^{2}
7	2.7×10^{1}	2.6×10^{2}	7.5×10^{2}	-1.3×10^{3}	6.2×10^{3}
8	6.7×10^{1}	7.5×10^{2}	2.6×10^{3}	-3.4×10^{3}	1.5×10^{4}
9	-1.2×10^{2}	-1.3×10^{3}	-3.4×10^{3}	8.0×10^{3}	-4.2×10^{4}
10	5.8×10^{2}	6.2×10^{3}	1.5×10^{4}	-4.2×10^{4}	2.3×10^{5}
11	-3.3×10^{-2}	-4.1×10^{-1}	-2.3	-4.3×10^{-1}	8.5
12	-1.1×10^{-4}	-8.8×10^{-4}	-3.8×10^{-3}	-1.3×10^{-3}	1.4×10^{-2}
13	6.2	6.8×10^{1}	3.4×10^{2}	-3.2×10^{1}	-6.8×10^{2}
14	2.6×10^{1}	-1.8×10^{1}	-5.7×10^{2}	3.0×10^{2}	-3.5×10^{2}
15	-7.4×10^{-1}	3.8×10^{1}	2.7×10^{2}	-4.1×10^{1}	-4.1×10^{2}

Σ_{ij}	11	12	13	14	15
1	-3.0×10^{-6}	4.6×10^{-7}	9.6×10^{-4}	-2.3×10^{-2}	-4.7×10^{-3}
2	8.9×10^{-4}	-9.8×10^{-6}	-2.3×10^{-1}	6.1×10^{-1}	1.0×10^{-1}
3	1.1×10^{-2}	-6.5×10^{-4}	-1.5×10^{1}	2.3×10^{1}	-9.0
4	-3.9×10^{-1}	-2.3×10^{-3}	1.8×10^{1}	6.7	3.2×10^{1}
5	5.6×10^{-1}	1.6×10^{-2}	2.1×10^{2}	-4.7×10^{2}	1.7×10^{1}
6	-3.3×10^{-2}	-1.1×10^{-4}	6.2	2.6×10^{1}	-7.4×10^{-1}
7	-4.1×10^{-1}	-8.8×10^{-4}	6.8×10^{1}	-1.8×10^{1}	3.8×10^{1}
8	-2.3	-3.8×10^{-3}	3.4×10^{2}	-5.7×10^{2}	2.7×10^{2}
9	-4.3×10^{-1}	-1.3×10^{-3}	-3.2×10^{1}	3.0×10^{2}	-4.1×10^{1}
10	8.5	1.4×10^{-2}	-6.8×10^{2}	-3.5×10^{2}	-4.1×10^{2}
11	6.8×10^{-3}	1.2×10^{-5}	-8.2×10^{-1}	9.2×10^{-1}	-6.1×10^{-1}
12	1.2×10^{-5}	4.5×10^{-4}	-1.2×10^{-3}	-4.2×10^{-3}	7.4×10^{-5}
13	-8.2×10^{-1}	-1.2×10^{-3}	1.2×10^{2}	-1.9×10^{2}	1.1×10^{2}
14	9.2×10^{-1}	-4.2×10^{-3}	-1.9×10^{2}	1.9×10^{3}	-5.4×10^{2}
15	-6.1×10^{-1}	7.4×10^{-5}	1.1×10^{2}	-5.4×10^{2}	2.8×10^{2}

[1] N. Schunck, *Energy Density Functional Methods for Atomic Nuclei* (IOP Publishing, Bristol, 2019), pp. 2053–2563.

[2] G. Grams, N. N. Shchechilin, A. Sánchez-Fernández, W. Ryssens, N. Chamel, and S. Goriely, Skyrme–Hartree–Fock–Bogoliubov mass models on a 3D mesh: IV. Improved description of the isospin dependence of pairing, Eur. Phys. J. A **61**, 35 (2025).

[3] G. Grams, W. Ryssens, A. Sánchez-Fernández, N. N. Shchechilin, L. G.-M. Zaragoza, P. Demol, N. Chamel, S. Goriely, and M. Bender, Skyrme-Hartree-Fock-Bogoliubov

mass models on a 3D mesh V. The N2LO extension of the Skyrme EDF, Phys. Lett. B **879**, 140590 (2026).
[4] L. Scurto, H. Pais, and F. Gulminelli, General predictions of neutron star properties using unified relativistic mean-field equations of state, Phys. Rev. D **109**, 103015 (2024).
[5] P. Char and C. Mondal, Exploring the limits of nucleonic metamodeling using different relativistic density functionals, Phys. Rev. D **111**, 103024 (2025).
[6] H. Dinh Thi, C. Mondal, and F. Gulminelli, The nuclear matter density functional under the nucleonic hypothesis, Universe **7**, 373 (2021).
[7] M. V. Beznogov and A. R. Raduta, Bayesian inference of the dense matter equation of state built upon extended Skyrme interactions, Phys. Rev. C **110**, 035805 (2024).
[8] X. Roca-Maza and N. Paar, Nuclear equation of state from ground and collective excited state properties of nuclei, Prog. Part. Nucl. Phys. **101**, 96 (2018).
[9] R. Kumar, V. Dexheimer, J. Jahan, J. Noronha, J. Noronha-Hostler, C. Ratti, N. Yunes, A. R. Nava Acuna, M. Alford, M. H. Anik, D. Chatterjee, K. Chatziioannou, H.-Y. Chen, A. Clevinger, C. Conde, N. Cruz-Camacho, T. Dore, C. Drischler, H. Elfner, R. Essick, *et al.*, Theoretical and experimental constraints for the equation of state of dense and hot matter, Living Rev. Relativity **27**, 3 (2024).
[10] E. Yüksel, T. Marketin, and N. Paar, Optimizing the relativistic energy density functional with nuclear ground state and collective excitation properties Phys. Rev. C **99**, 034318 (2019).
[11] Z. Zhang and L.-W. Chen, Bayesian inference of the symmetry energy and the neutron skin in ^{48}Ca and ^{208}Pb from CREX and PREX-2, Phys. Rev. C **108**, 024317 (2023).
[12] J. Xu and P. Papakonstantinou, Bayesian inference of finite-nuclei observables based on the KIDS model Phys. Rev. C **105**, 044305 (2022).
[13] J. Erler, N. Birge, M. Kortelainen, W. Nazarewicz, E. Olsen, A. M. Perhac, and M. Stoitsov, The limits of the nuclear landscape, Nature (London) **486**, 509 (2012).
[14] P. Klausner, G. Colò, X. Roca-Maza, and E. Vigezzi, Impact of ground-state properties and collective excitations on the Skyrme ansatz: A Bayesian study, Phys. Rev. C **111**, 014311 (2025).
[15] P. Klausner, M. Antonelli, and F. Gulminelli, Properties of the neutron star crust informed by nuclear structure data, Phys. Rev. C **113**, 025808 (2026).
[16] C. E. Rasmussen and C. K. I. Williams, *Gaussian Processes for Machine Learning* (MIT Press, Cambridge, 2006).
[17] MADAI collaboration (Models and D. A. Initiative), http://madai.phy.duke.edu/.
[18] J. Margueron, R. Hoffmann Casali, and F. Gulminelli, Equation of state for dense nucleonic matter from metamodeling. I. Foundational aspects, Phys. Rev. C **97**, 025805 (2018).
[19] P. Landry and R. Essick, Nonparametric inference of the neutron star equation of state from gravitational wave observations, Phys. Rev. D **99**, 084049 (2019).
[20] R. Essick, P. Landry, and D. E. Holz, Nonparametric inference of neutron star composition, equation of state, and maximum mass with GW170817, Phys. Rev. D **101**, 063007 (2020).
[21] J. S. Read, B. D. Lackey, B. J. Owen, and J. L. Friedman, Constraints on a phenomenologically parametrized neutron-star equation of state, Phys. Rev. D **79**, 124032 (2009).
[22] L. Suleiman, M. Fortin, J. L. Zdunik, and C. M. C. Providência, Polytropic fits of modern and unified equations of state, Phys. Rev. C **106**, 035805 (2022).
[23] E. Chabanat, P. Bonche, P. Haensel, J. Meyer, and R. Schaeffer, A Skyrme parametrization from subnuclear to neutron star densities, Nucl. Phys. A **627**, 710 (1997).
[24] L.-W. Chen, B.-J. Cai, C. M. Ko, B.-A. Li, C. Shen, and J. Xu, Higher-order effects on the incompressibility of isospin asymmetric nuclear matter, Phys. Rev. C **80**, 014322 (2009).
[25] L.-W. Chen, C. M. Ko, B.-A. Li, and J. Xu, Density slope of the nuclear symmetry energy from the neutron skin thickness of heavy nuclei Phys. Rev. C **82**, 024321 (2010).
[26] P. Ring, P. Schuck, and M. R. Strayer, The nuclear many-body problem, Phys. Today **36**(7), 70 (1983).
[27] W. Satuła and R. Wyss, Competition between $T = 0$ and $T = 1$ pairing in proton-rich nuclei, Phys. Lett. B **393**, 1 (1997).
[28] W. Satuła, D. Dean, J. Gary, S. Mizutori, and W. Nazarewicz, On the origin of the Wigner energy, Phys. Lett. B **407**, 103 (1997).
[29] W. Satuła and R. Wyss, A number projected model with generalized pairing interaction, Nucl. Phys. A **676**, 120 (2000).
[30] M. Wang, W. Huang, F. Kondev, G. Audi, and S. Naimi, The AME 2020 atomic mass evaluation (II). Tables, graphs and references, Chin. Phys. C **45**, 030003 (2021).
[31] I. Angeli and K. Marinova, Table of experimental nuclear ground state charge radii: An update, At. Data Nucl. Data Tables **99**, 69 (2013).
[32] W. Satuła, J. Dobaczewski, and W. Nazarewicz, Odd-even staggering of nuclear masses: Pairing or shape effect? Phys. Rev. Lett. **81**, 3599 (1998).
[33] Y. K. Gupta, K. B. Howard, U. Garg, J. T. Matta, M. Şenyiğit, M. Itoh, S. Ando, T. Aoki, A. Uchiyama, S. Adachi, M. Fujiwara, C. Iwamoto, A. Tamii, H. Akimune, C. Kadono, Y. Matsuda, T. Nakahara, T. Furuno, T. Kawabata, M. Tsumura, *et al.*, Isoscalar giant monopole, dipole, and quadrupole resonances in ^{90,92}Zr and ^{92}Mo, Phys. Rev. C **97**, 064323 (2018).
[34] Y. Gupta, U. Garg, K. Howard, J. Matta, M. Şenyiğit, M. Itoh, S. Ando, T. Aoki, A. Uchiyama, S. Adachi, M. Fujiwara, C. Iwamoto, A. Tamii, H. Akimune, C. Kadono, Y. Matsuda, T. Nakahara, T. Furuno, T. Kawabata, M. Tsumura, *et al.*, Are there nuclear structure effects on the isoscalar giant monopole resonance and nuclear incompressibility near A ~ 90, Phys. Lett. B **760**, 482 (2016).
[35] J. A. Melendez, R. J. Furnstahl, D. R. Phillips, M. T. Pratola, and S. Wesolowski, Quantifying correlated truncation errors in effective field theory, Phys. Rev. C **100**, 044001 (2019).
[36] G. Colò, L. Cao, N. Van Giai, and L. Capelli, Self-consistent RPA calculations with Skyrme-type interactions: The skyrme_rpa program, Comput. Phys. Commun. **184**, 142 (2013).
[37] G. Colò and X. Roca-Maza, User guide for the hfbcs-qrpa(v1) code, arXiv:2102.06562.
[38] M. Kortelainen, T. Lesinski, J. Moré, W. Nazarewicz, J. Sarich, N. Schunck, M. V. Stoitsov, and S. Wild, Nuclear energy density optimization Phys. Rev. C **82**, 024313 (2010).
[39] P. Möller, W. D. Myers, H. Sagawa, and S. Yoshida, New finite-range droplet mass model and equation-of-state parameters Phys. Rev. Lett. **108**, 052501 (2012).
[40] S. Shlomo, V. M. Kolomietz, and G. Colò, Deducing the nuclear-matter incompressibility coefficient from data on isoscalar compression modes, Eur. Phys. J. A **30**, 23 (2006).
[41] E. Khan, J. Margueron, and I. Vidaña, Constraining the nuclear equation of state at subsaturation densities Phys. Rev. Lett. **109**, 092501 (2012).

[42] B.-A. Li, B.-J. Cai, W.-J. Xie, and N.-B. Zhang, Progress in constraining nuclear symmetry energy using neutron star observables since GW170817, Universe **7**, 182 (2021).

[43] P.-G. Reinhard, X. Roca-Maza, and W. Nazarewicz, Combined theoretical analysis of the parity-violating asymmetry for ^{48}Ca and ^{208}Pb, Phys. Rev. Lett. **129**, 232501 (2022).

[44] X. Roca-Maza, M. Brenna, G. Colò, M. Centelles, X. Viñas, B. K. Agrawal, N. Paar, D. Vretenar, and J. Piekarewicz, Electric dipole polarizability in ^{208}Pb: Insights from the droplet model, Phys. Rev. C **88**, 024316 (2013).

[45] X. Roca-Maza, X. Viñas, M. Centelles, B. K. Agrawal, G. Colò, N. Paar, J. Piekarewicz, and D. Vretenar, Neutron skin thickness from the measured electric dipole polarizability in ^{68}Ni, ^{120}Sn, and ^{208}Pb, Phys. Rev. C **92**, 064304 (2015).

[46] T.-G. Yue, Z. Zhang, and L.-W. Chen, PREX and CREX: Evidence for strong isovector spin-orbit interaction, Sci. Bull. **71**, 1270 (2026).

[47] T. Zhao, Z. Lin, B. Kumar, A. W. Steiner, and M. Prakash, Characterizing the nuclear models informed by PREX and CREX: A view from Bayesian inference, Phys. Rev. Res. **7**, 043335 (2025).

[48] M. Qiu, T.-G. Yue, Z. Zhang, and L.-W. Chen, A relativistic mechanism for the enhanced isovector spin-orbit interaction suggested by parity-violating electron scattering experiments, Phys. Lett. B **879**, 140648 (2026).

[49] A. Kunjipurayil, J. Piekarewicz, and M. Salinas, Role of the isovector spin-orbit potential in mitigating the CREX-PREX dilemma, Phys. Rev. C **112**, 014310 (2025).

[50] M. Salinas and J. Piekarewicz, Impact of tensor couplings with scalar mixing on covariant energy density functionals, Phys. Rev. C **109**, 045807 (2024).

[51] P. Papakonstantinou, CREX and PREX-II reconciled within energy-density functional theory, arXiv:2602.22722.

[52] G. Montefusco, M. Antonelli, and F. Gulminelli, Frozen and β-equilibrated f and p modes of cold neutron stars: Nuclear metamodel predictions A& A **694**, A150 (2025).

[53] A. Saffer, E. Fonseca, S. Ransom, I. Stairs, R. Lynch, D. Good, K. W. Masui, J. W. McKee, B. W. Meyers, S. S. Patil, and C. M. Tan, A lower mass estimate for PSR J0348 + 0432 based on CHIME/Pulsar precision timing, Astrophys. J. Lett. **983**, L20 (2025).

[54] J. Antoniadis, P. C. C. Freire, N. Wex, T. M. Tauris, R. S. Lynch, M. H. van Kerkwijk, M. Kramer, C. Bassa, V. S. Dhillon, T. Driebe, J. W. T. Hessels, V. M. Kaspi, V. I. Kondratiev, N. Langer, T. R. Marsh, M. A. McLaughlin, T. T. Pennucci, S. M. Ransom, I. H. Stairs, J. van Leeuwen, *et al.*, A massive pulsar in a compact relativistic binary, Science **340**, 1233232 (2013).

[55] E. Fonseca, H. T. Cromartie, T. T. Pennucci, P. S. Ray, A. Y. Kirichenko, S. M. Ransom, P. B. Demorest, I. H. Stairs, Z. Arzoumanian, L. Guillemot, A. Parthasarathy, M. Kerr, I. Cognard, P. T. Baker, H. Blumer, P. R. Brook, M. DeCesar, T. Dolch, F. A. Dong, E. C. Ferrara, *et al.*, Refined mass and geometric measurements of the high-mass PSR J0740+6620, Astrophys. J. Lett. **915**, L12 (2021).

[56] J. M. Pearson, N. Chamel, A. Y. Potekhin, A. F. Fantina, C. Ducoin, A. K. Dutta, and S. Goriely, Unified equations of state for cold non-accreting neutron stars with Brussels–Montreal functionals – I. Role of symmetry energy Mon. Not. R. Astron. Soc. **481**, 2994 (2018).

[57] X. Roca-Maza and J. Piekarewicz, Impact of the symmetry energy on the outer crust of nonaccreting neutron stars, Phys. Rev. C **78**, 025807 (2008).

[58] H. Sotani, Shear oscillations in neutron stars and the nuclear symmetry energy Phys. Rev. D **109**, 023030 (2024).

[59] N. A. Zemlyakov and A. I. Chugunov, Neutron star inner crust: Reduction of shear modulus by nuclei finite size effect, Mon. Not. R. Astron. Soc. **518**, 3813 (2023).

[60] N. A. Zemlyakov and A. I. Chugunov, Constraining the shear modulus of a polycrystalline neutron star crust: Hashin-Shtrikman variational approach, Phys. Rev. D **112**, 043032 (2025).

[61] M. C. Miller, F. K. Lamb, A. J. Dittmann, S. Bogdanov, Z. Arzoumanian, K. C. Gendreau, S. Guillot, W. C. G. Ho, J. M. Lattimer, M. Loewenstein, S. M. Morsink, P. S. Ray, M. T. Wolff, C. L. Baker, T. Cazeau, S. Manthripragada, C. B. Markwardt, T. Okajima, S. Pollard, I. Cognard, *et al.*, The radius of PSR J0740+6620 from NICER and XMM-Newton data, Astrophys. J. Lett. **918**, L28 (2021).

[62] D. Choudhury, T. Salmi, S. Vinciguerra, T. E. Riley, Y. Kini, A. L. Watts, B. Dorsman, S. Bogdanov, S. Guillot, P. S. Ray, D. J. Reardon, R. A. Remillard, A. V. Bilous, D. Huppenkothen, J. M. Lattimer, N. Rutherford, Z. Arzoumanian, K. C. Gendreau, S. M. Morsink, and W. C. G. Ho, A NICER view of the nearest and brightest millisecond pulsar: PSR J0437–4715, Astrophys. J. Lett. **971**, L20 (2024).

[63] S. Vinciguerra, T. Salmi, A. L. Watts, D. Choudhury, T. E. Riley, P. S. Ray, S. Bogdanov, Y. Kini, S. Guillot, D. Chakrabarty, W. C. G. Ho, D. Huppenkothen, S. M. Morsink, Z. Wadiasingh, and M. T. Wolff, An updated mass–radius analysis of the 2017–2018 NICER data set of PSR J0030+0451, Astrophys. J. **961**, 62 (2024).

[64] L. Mauviard, S. Guillot, T. Salmi, D. Choudhury, B. Dorsman, D. González-Caniulef, M. Hoogkamer, D. Huppenkothen, C. Kazantsev, Y. Kini, J.-F. Olive, P. Stammler, A. L. Watts, M. Mendes, N. Rutherford, A. Schwenk, I. Svensson, S. Bogdanov, M. Kerr, P. S. Ray, *et al.*, A NICER view of the 1.4 $M_{\odot}$ edge-on pulsar PSR J0614-3329, Astrophys. J. **995**, 60 (2025).

[65] See Supplemental Material at http://link.aps.org/supplemental/10.1103/p6xt-x2zp for files containing numerical values of Tables V and VI.

[66] N. Rutherford, M. Mendes, I. Svensson, A. Schwenk, A. L. Watts, K. Hebeler, J. Keller, C. Prescod-Weinstein, D. Choudhury, G. Raaijmakers, T. Salmi, P. Timmerman, S. Vinciguerra, S. Guillot, and J. M. Lattimer, Constraining the dense matter equation of state with new NICER mass–radius measurements and new chiral effective field theory inputs, Astrophys. J. Lett. **971**, L19 (2024).

[67] H. Gil, Y. Oh, C. H. Hyun, and P. Papakonstantinou, Skyrme-type nuclear force for the KIDS energy density functional, New Phys.: Sae Mulli **67**, 456 (2017).

[68] H. Gil, P. Papakonstantinou, C. H. Hyun, T. S. Park, and Y. Oh, Acta Phys. Pol. B **48**, 305 (2017).

[69] P. Papakonstantinou, T.-S. Park, Y. Lim, and C. H. Hyun, Density dependence of the nuclear energy-density functional Phys. Rev. C **97**, 014312 (2018).

[70] S. A. Fayans, Towards a universal nuclear density functional, Pis'ma Zh. Éksp. Teor. Fiz. **68**, 161 (1998) [JETP Lett. **68**, 169 (1998)].